Antisolar differential rotation with surface lithium enrichment on the single K-giant V1192 Ori ⋆

Zs. Kővári[1], K. G. Strassmeier[2], T. A. Carroll[2], K. Oláh[1], L. Kriskovics[1], E. Kővári[3], O. Kovács[1, 3], K. Vida[1],
T. Granzer[2], and M. Weber[2]

[1] Konkoly Observatory, Research Centre for Astronomy and Earth Sciences, Hungarian Academy of Sciences, Konkoly Thege út 15-17., H-1121, Budapest, Hungary
e-mail: `kovari@konkoly.hu`
[2] Leibniz-Institute for Astrophysics Potsdam (AIP), An der Sternwarte 16, D-14482 Potsdam, Germany
[3] Eötvös University, Department of Astronomy, Pf. 32., H-1518, Budapest, Hungary

ABSTRACT

Context. Stars with about 1−2 solar masses at the red giant branch (RGB) represent an intriguing period of stellar evolution, i.e. when the convective envelope interacts with the fast-rotating core. During these mixing episodes freshly synthesized lithium can come up to the stellar surface along with high angular momentum material. This high angular momentum may alter the surface rotation pattern.
Aims. The single rapidly rotating K-giant V1192 Ori is revisited to determine its surface differential rotation, lithium abundance, and basic stellar properties such as a precise rotation period. The aim is to independently verify the antisolar differential rotation of the star and possibly find a connection to the surface lithium abundance.
Methods. We applied time-series Doppler imaging to a new multi-epoch data set. Altogether we reconstructed 11 Doppler images from spectroscopic data collected with the STELLA robotic telescope between 2007–2016. We used our inversion code *iMap* to reconstruct all stellar surface maps. We extracted the differential rotation from these images by tracing systematic spot migration as a function of stellar latitude from consecutive image cross-correlations.
Results. The position of V1192 Ori in the Hertzsprung-Russell diagram suggests that the star is in the helium core-burning phase just leaving the RGB bump. We measure $A(\mathrm{Li})_{\mathrm{NLTE}} = 1.27$, i.e. a value close to the anticipated transition value of 1.5 from Li-normal to Li-rich giants. Doppler images reveal extended dark areas arranged quasi-evenly along an equatorial belt. No cool polar spot is found during the investigated epoch. Spot displacements clearly suggest antisolar surface differential rotation with $\alpha = -0.11 \pm 0.02$ shear coefficient.
Conclusions. The surface Li enrichment and the peculiar surface rotation pattern may indicate a common origin.

Key words. stars: activity – stars: imaging – stars: late-type – stars: starspots – stars: individual: V1192 Ori

1. Introduction

Stellar magnetic activity manifests itself in cool starspots on the stellar surface and is strongly related to rapid rotation. Although most of the stellar angular momentum is supposed to be transferred to its environment by a wind and consequent magnetic braking on the main sequence, there are examples of evolved red giant branch (RGB) stars that are still rapidly rotating and magnetically active. Most of these are members of close binary systems in which tidal forces maintain fast rotation. Rapidly rotating single giants remain a challenge for angular-momentum evolution theories. There are scenarios that allow a star to keep its angular momentum after the main sequence, such as enhanced mixing and dredge-up episodes (Simon & Drake 1989; Charbonnel & Lagarde 2010) or planet engulfment (Privitera et al. 2016b).

After the main sequence, RGB stars of about 1−2 solar masses represent an intriguing episode of stellar evolution. When the deepening convective envelope interacts with the fast-rotating core, angular momentum is transported to the surface.

The mixing of the envelope material with the hotter layers below infer the decay of light elements. This short evolutionary period called the first dredge up is responsible for the dilution of the surface lithium. Despite the expected low lithium abundance, a handful of low-mass stars in this evolutionary state show lithium enrichment on their surfaces. For intermediate mass ($\approx4-7\,M_\odot$) stars at the asymptotic giant branch (AGB), the Cameron–Fowler mechanism (Cameron & Fowler 1971) followed by a transport of the Li to cooler regions can plausibly explain the lithium excess. On the other hand, for lower masses at the RGB this mechanism may not work and other non-standard extra mixing processes are required (cf. Sackmann & Boothroyd 1992; Charbonnel & Lagarde 2010). In turn, cool-bottom processes (Wasserburg et al. 1995; Sackmann & Boothroyd 1999) below the convection zone may also be capable for transporting material to layers hot enough for the Cameron–Fowler mechanism and then returning to the convection zone. An alternative evolutionary model was proposed by de La Reza et al. (1996) in which basically every low-mass K-giant undergoes a short ($\approx10^5$ yr) Li-rich phase on the RGB (see also de la Reza et al. 1997; Kirby et al. 2016). Extra non-axisymmetric mixing that leads to an inhomogeneous super-granulation pattern on the surface in the

---

form of large cool and warm features was invoked to explain super-meteoritic Li abundances in Strassmeier et al. (2015).

So far, differential rotation is found to be solar type for main-sequence stars, but giant stars can exhibit antisolar differential rotation, i.e. the equator rotates more slowly than the poles (Vogt & Hatzes 1991; Strassmeier et al. 2003; Kővári et al. 2015, etc.). Theoretically, this phenomenon is induced and maintained by strong meridional circulation (Kitchatinov & Rüdiger 2004). Aurnou et al. (2007) proposed that strong mixing by turbulent convection would be the primary agent for angular momentum equilibration and thus antisolar differential rotation. Detailed numerical simulations by, for example Käpylä et al. (2014) and Gastine et al. (2014), suggest that rapidly rotating stars with a small Rossby number yield solar-like differential rotation, while weakly rotating stars with large Rossby numbers may sustain antisolar differential rotation. On the other hand, only three single rapidly rotating giants are known so far to exhibit antisolar differential rotation, namely DI Psc, DP CVn (Kővári et al. 2013), and V1192 Ori (Strassmeier et al. 2003, the star revisited in this paper).

Interestingly, these stars are listed among the very few fast-rotating RGB stars with unusually high surface lithium abundances (see Table 1 in Charbonnel & Balachandran 2000), implying a possible connection between the antisolar differential rotation profile and the enhanced surface lithium (Kriskovics et al. 2014). We posit whether it is possible that a yet-unknown mixing mechanism responsible for the lithium enrichment can eventually also alter the surface differential rotation profile to be antisolar. We believe that such fast-rotating, single, RGB stars provide a good opportunity to investigate the relationship between activity, rotation, differential rotation, and surface lithium abundance.

In this paper, we present a time-series Doppler imaging study of the single rapidly rotating ($P_{\rm rot} \approx 28$ days) K-giant V1192 Ori (=HD 31993), based on spectroscopic observations from the STELLA robotic observatory in Tenerife (Strassmeier et al. 2010). The star was found to have strong Ca II H&K emission and was classified as a K2 giant (Bidelman & MacConnell 1973; Fekel et al. 1986; Strassmeier et al. 1990) with an unusually high $v \sin i$ value of 31 km s^{-1} (see also Fekel 1997; Fekel & Balachandran 1993). V1192 Ori was catalogued as Li-rich according to its lithium abundance, which is substantially larger than expected for an ordinary K giant (Fekel 1988). The non-local thermodynamic equilibrium (NLTE) lithium abundance for V1192 Ori was measured as $A(\rm Li) = 1.4 \pm 0.2$ (Fekel & Balachandran 1993) on the usual logarithmic scale, i.e. just at the border of $A(\rm Li) \geq 1.5$ between Li-normal and Li-rich giants (cf. Charbonnel & Balachandran 2000). Castilho et al. (2000) found $A(\rm Li)$ of 1.7 assuming local thermodynamic equilibrium (LTE), and 1.8 with NLTE correction. More recently, Rebull et al. (2015) quoted the star as Li-normal with $A(\rm Li) = 1.26$ under NLTE assumption.

V1192 Ori shows a wide range of magnetic-activity indicators from X-ray to infrared (but remains undetected in radio; see Slee et al. 1987). The star was listed as an X-ray source by the *Einstein* and ROSAT surveys (Gioia et al. 1990; Voges et al. 1999, respectively). International Ultraviolet Explorer (IUE) observations revealed an active UV chromosphere (Fekel & Balachandran 1993) in accordance with the photospheric light variability (Strassmeier et al. 1997a, 1999), which is attributed to stellar rotation and cool starspots. According to the Zeeman signatures detected by Aurière et al. (2015), V1192 Ori possesses a strong surface magnetic field that is likely produced by an $\alpha\Omega$-type dynamo. The star is also listed in the IRAS (Gezari et al.

1999) and 2MASS (Cutri et al. 2003) infrared point source catalogues.

The first comprehensive photometric and spectroscopic study of V1192 Ori was carried out by (Strassmeier et al. 2003, hereafter Paper I). A rotational period of ≈26 days was derived from the photometric variability which, together with $v \sin i$ of 32 km s^{-1}, suggested a minimum radius of ≈16 $R_\odot$ that is consistent with the K2 giant classification. The comparison of the position of V1192 Ori in the Hertzsprung-Russell (H-R) diagram with feasible evolutionary tracks yielded a mass determination of 1.9 $M_\odot$. In Paper I two Doppler images were presented for consecutive rotation periods showing cool starspots mostly at low to mid-latitudes. Surface differential rotation was investigated by cross-correlating the subsequent maps and yielded antisolar differential rotation. Such observations are relevant constraints for dynamo theory, hence their reliability is of great consequence. Therefore, we revisit V1192 Ori and carry out a new, more detailed Doppler-imaging study from new high-quality spectroscopic data.

The paper is organized as follows. In Sect. 2 we describe the observations and in Sect. 3 provide a more accurate photometric period from the available photometric data. The astrophysical data are summarized in Sect. 4, where we also present a redetermination of the surface lithium abundance. In Sect. 6, we focus on the time-series Doppler imaging. The results are summarized and discussed in Sect. 8.

2. Observations

2.1. Photometry

Two data sets for V1192 Ori were obtained. The first part of the observations was collected between February 1993–March 1997 (JD 2,449,024–2,450,537), while the second part was obtained between March 2007–December 2014 (JD 2,454,173–2,457,003). All observations were carried out with the T7 ('Amadeus') 0.75 m automatic photoelectric telescope (APT) at Fairborn Observatory in southern Arizona (Strassmeier et al. 1997b), which is currently owned and operated by the Leibniz-Institute for Astrophysics Potsdam (AIP); see Granzer et al. (2001) for more details. The two data sets consist of altogether 1312 measurements in Johnson-Cousins V and I_C. HD 32191 ($V = 8^{\rm m}520 \pm 0^{\rm m}015$, $I_C = 7^{\rm m}287 \pm 0^{\rm m}021$) was used as a comparison star while HD 32073 was used as the check star. Typical data quality is around 6 mmag rms in the first data set but significantly worse in the second because of a defocussing problem. The photometric V data are plotted in Fig. 1.

2.2. Spectroscopy

A total of 460 high-resolution echelle spectra were recorded with the 1.2 m STELLA robotic observatory (Strassmeier et al. 2010) at the Izaña Observatory in Tenerife, Spain, between Jan 9, 2007 and Feb 3, 2016. The telescope is equipped with the fibre-fed, fixed-format STELLA Echelle Spectrograph (SES). The spectra cover the full 3900–8800 Å wavelength range with an average spectral resolution of $R = 55\,000$. Further details on the performance of the system and the data reduction procedures can be found in Weber et al. (2008, 2012) and Weber & Strassmeier (2011). Table A.1 in the Appendix gives the log of the SES observations used for the Doppler reconstructions presented in Sect. 6.
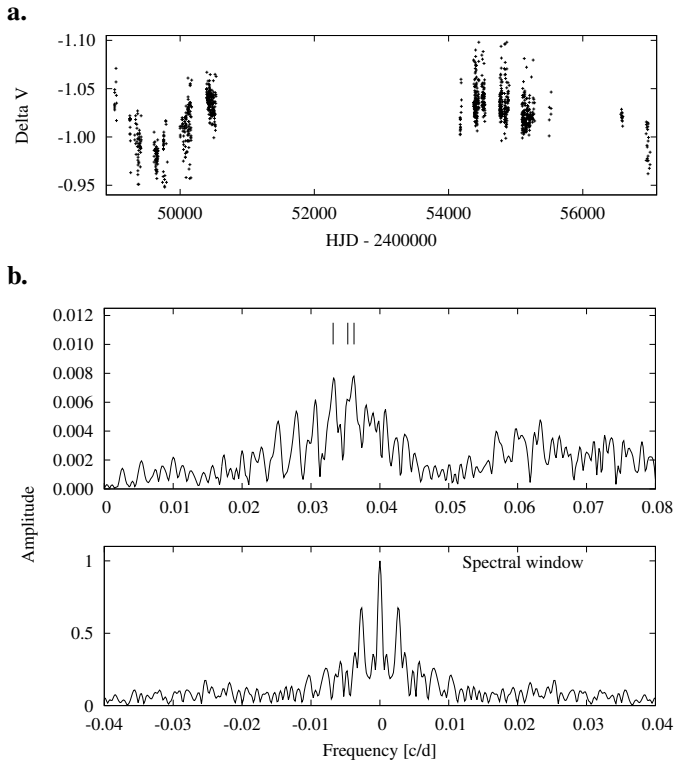
a.

b.

Fig. 1. a. Long-term photometric V data of V1192 Ori observed with the Amadeus APT. **b.** Amplitude spectrum (top) and spectral window (bottom) from the Johnson V data obtained between 1993–1997. The three most significant period signals are indicated. See text for details.

Table 1. Multi-component Fourier-fit parameters

Frequency [c/d]	Amplitude	Residual	Residual difference
$f_1 = 0.036250$	0.00777	0.012761	
$f_1 = 0.036214$	0.01034		
$f_2 = 0.032574$	0.00819	0.011528	0.001233
$f_1 = 0.036236$	0.00922		
$f_2 = 0.033289$	0.00648		
$f_3 = 0.035346$	0.01090	0.010278	0.001250
$f_1 = 0.036394$	0.00658		
$f_2 = 0.033197$	0.00928		
$f_3 = 0.035302$	0.00940		
$f_4 = 0.030785$	0.00556	0.009997	0.000281

By interpreting the three period peaks as a sign of surface differential rotation, we obtained a surface shear parameter $\Delta P/P$ of ≈ 0.09. This shear parameter is within the error box of the value derived from consecutive Doppler images in Paper I. From photometric time series alone one cannot determine the sign of the surface shear, that is, whether the differential rotation is solar type or antisolar, but see Reinhold & Arlt (2015) for long-term space photometry.

The new photometric period is longer by $\approx 10\%$ compared to that from Paper I and is based on a data set that is roughly four times longer. The 2f harmonic of 13.9 d in Paper I also indicated a longer period of around 28 d. The second, more noisy part of the data between March 2007–December 2014 yields a 31.8 d period but with a very low significance. Putting together all the available photometric data results in an ≈ 28 d period. Therefore, we accept $P_{\mathrm{rot}} = 28.30$ d from the first data set as the most feasible and accurate rotation period. Accordingly, for phase calculations we use the following equation:

$$\mathrm{HJD} = 2,450,369.2 + 28.30 \times E, \qquad (1)$$

where the reference time was chosen arbitrarily (cf. Paper I).

3. Photometric period

Using the Fourier transformation-based frequency analyser code MuFrAn (Csubry & Kolláth 2004) we analysed the V data of V1192 Ori to refine the photometric period. In Paper I, only the 1996-1997 APT data were used for the period search, yielding in principle the correct but ambiguous and uncertain period of 25.3 d.

The quality of the new photometric data turned out to be very uneven between the two sets of observations (see Sect. 2.1). We found that the second set from March 2007–December 2014 is rather noisy compared to the first set from February 1993–March 1997. Moreover, the rotational variation of V1192 Ori has usually low amplitude. Therefore, we used only the first data part for the period analysis. The resulting amplitude spectrum is shown in Fig. 1. For the refinement of the period we took the three highest peaks and perform a multi-periodic fit. From this the highest amplitude belongs to the 28.3 d period (middle tick mark in the top panel of Fig. 1). We confirmed this period by consecutively pre-whitening with the three periods. Finally, we settled on $P_{\mathrm{phot}} = 28.30 \pm 0.02$ d. The other significant periods denoted by the other tick marks are 27.59 d and 30.06 d. Owing to the crosstalk between the neighbouring peaks, it is not evident that the highest amplitude peak corresponds to the middle tick. Therefore, in Table 1 we listed the frequencies, amplitudes and residuals of 1-, 2-, 3- and 4-component Fourier-fits carried out subsequently. The residuals decrease significantly until the 3-component fit, however, introducing the 4th component yields only marginal improvement. In the 3- and 4-component fits the highest amplitudes correspond to ≈ 0.0353 c/d, i.e. ≈ 28.3 days period.

4. Fundamental parameters

We redetermined the effective temperature (T_{eff}), surface gravity ($\log g$), metallicity ([Fe/H]), and projected rotational velocity ($v \sin i$) via the spectrum-synthesis code ParSES (Allende Prieto 2004; Jovanovic et al. 2013) implemented in the standard STELLA-SES data reduction process (Weber et al. 2008). For the synthetic spectra, we determined a microturbulence ξ_{mic} of 1.25 km s^{-1} by following the empirical relation as was used in the Gaia-ESO survey (Jofré et al. 2014). The radial-tangential macroturbulence ξ_{mac} of 3 km s^{-1} was taken from Fekel (1997), but see also Paper I. The resulting parameters with their internal standard deviations are listed in Table 2. When compared to the previous values in Paper I, the gravity $\log g$ and $v \sin i$ are only slightly different; these values are still within the small error boxes, but the effective temperature of 4305 K is lower by ≈ 200 K. However, the new, lower, value is in a better agreement with the colour-index temperature calibration by Worthey & Lee (2011) when taking $V - I_C = 1^{\mathrm{m}}33$ from the long-term photometric data. In Paper I $V - I = 1^{\mathrm{m}}21$ was taken from the Hipparcos/Tycho catalogue, which would have been in accordance with a temperature of ≈ 4400 K.

The photometric period of 28.3 d together with the projected rotational velocity of 32.0 ± 1.5 km s^{-1}, and taking 65° inclination
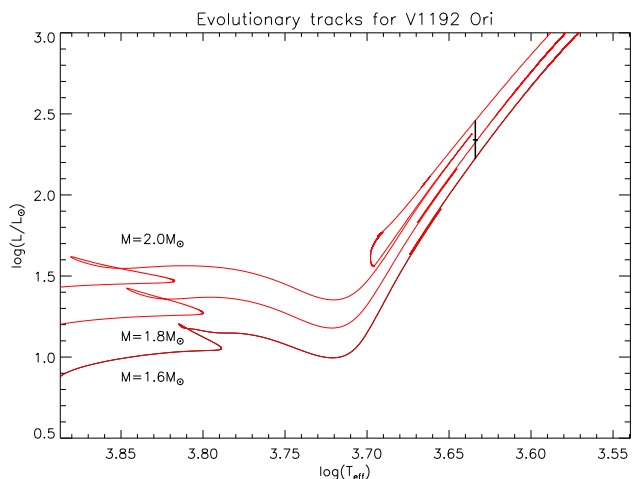
Fig. 2. Position of V1192 Ori (dot) in the H-R diagram. Shown are stellar evolutionary tracks for 1.6, 1.8, and 2.0 $M_\odot$ from *PARSEC*, assuming [Fe/H]=−0.08. The location of V1192 Ori at the RGB indicates a mass of 1.85 $M_\odot$ and an age of 1.6 Gyrs.

Fig. 3. Observed Li I 6708 Å spectral region of V1192 Ori fitted by synthetic Li profiles using LTE (green) and NLTE (blue) approximation.

Table 2. Astrophysical properties of V1192 Ori

Parameter	Value
Spectral type	K2.5 III
Distance$_{Gaia}$ [pc]	327^{+33}_{-28}
V_{br} [mag]	$7^m42 \pm 0^m10$
$(V - I)_{C,br}$ [mag]	$1^m33 \pm 0^m03$
M_{bol} [mag]	$-1^m10^{+0.29}_{-0.32}$
Luminosity [$L_\odot$]	218^{+73}_{-52}
$\log g$ [cgs]	2.39 ± 0.04
T_{eff} [K]	4305 ± 15
$v \sin i$ [km s^{-1}]	32.0 ± 1.5
Rotation period [d]	28.30 ± 0.02
Inclination [°]	65 ± 15
Radius [$R_\odot$]	$19.7^{+4.3}_{-2.1}$
Mass [$M_\odot$]	1.85 ± 0.30
Age [Gyr]	1.64 ± 0.3
Microturbulence [km s^{-1}]	1.25
Macroturbulence [km s^{-1}]	3.0
Metallicity [Fe/H]	-0.08 ± 0.02
NLTE Li abundance (log)	1.27 ± 0.15

from Paper I, yields a stellar radius $R = 19.7^{+4.4}_{-2.2}$ R$_\odot$ which, together with $T_{eff} = 4305$ K, fits fairly well for a K2.5 III classification (Dyck et al. 1996; van Belle et al. 1999). In Paper I a parameter study was carried out to select the true inclination by achieving the most homogeneous temperature inversion. For our new spectroscopic data we carried out a similar test with our new inversion code *iMap* (see Sect. 6.2) and obtained the most acceptable inversions for a range of inclination angles between 50°-70°. However, *iMap* works in a different way and is only of limited use to perform such a parameter search. Thus, we decided to keep the former inclination angle from Paper I assuming a slightly larger error bar of ±15°. From the radius and effective temperature it follows that the luminosity $L = 120^{+61}_{-26} L_\odot$. When assuming $M_{bol,\odot} = 4^m74$ this yields $M_{bol} = -0^m45^{+0.26}_{-0.46}$.

The improved parallax of 3.06±0.28 mas from *Gaia* DR1 (Gaia Collaboration et al. 2016b,a; Lindegren et al. 2016) yields a distance of 327^{+33}_{-28} pc, which is 25% larger compared to the *Hipparcos* distance of 238^{+83}_{-19} (cf. Paper I). Based on our long-
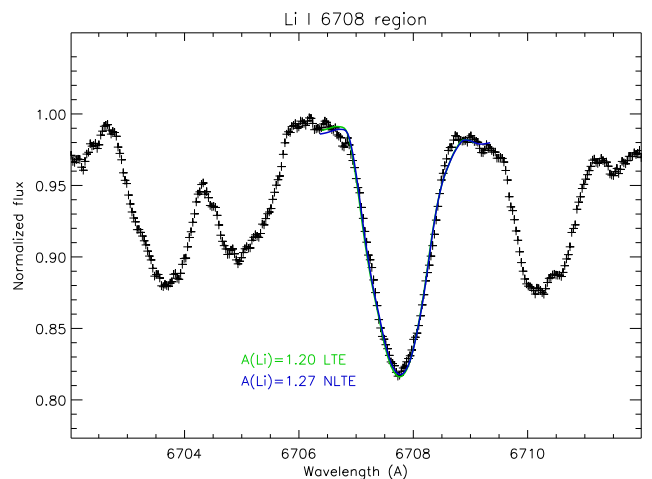
term APT photometry we are able to give a new estimation of $7^m42 \pm 0^m10$ for the brightest V magnitude observed so far (see V_{br} in Table 2). Taking these improved values and assuming an interstellar extinction of $A_V = 0^m191$ (Schlegel et al. 1998) together with a bolometric correction of $BC = -0^m76$ (Flower 1996) results in $M_{bol} = -1^m10^{+0.29}_{-0.32}$. This value and that calculated from T_{eff} and R agree with each other within their errors. The value M_{bol} derived from the *Gaia* parallax converts to a luminosity of $218^{+73}_{-52} L_\odot$, which we eventually adopted to find the most plausible position of V1192 Ori in the H-R diagram in Fig. 2. We adopted the *PARSEC* stellar evolution grid by Bressan et al. (2012, 2013), interpolating for [Fe/H] of −0.08 (Z=0.0157). From the model grid we obtained a mass of 1.85±0.3 $M_\odot$ with an age of 1.64±0.3 Gyr, typical for the epoch just after the RGB bump. This new mass is consistent with the value of 1.9±0.3 $M_\odot$ from Paper I. Taking the mass and radius would yield $\log g = 2.12^{+0.17}_{-0.27}$, i.e. a bit lower than the adopted value from ParSES. However, such a difference can originate from, for example a somewhat underestimated V_{br} (cf. Oláh et al. 2014), which would yield lower luminosity, therefore lower mass. Also, a 0.02 dex shift in metallicity yields a mass difference of ≈0.1.

5. Surface Li abundance

In Fig. 3 we plot an average Li I-6708 Å spectrum from summing up seven good-quality (S/N ratio of ≈200) spectra distributed evenly along all rotation phases in 2008. This spectrum yields S/N>500:1. For the abundance determination, we first employed SME spectral synthesis (Piskunov & Valenti 2017) with MARCS model atmospheres (Gustafsson et al. 2008) and with LTE approximation. Atomic data were gathered from the Vienna Atomic Line Database (VALD) (Kupka et al. 1999). The best fit resulted in A(Li) = 1.20, i.e. somewhat lower than the value of 1.4±0.2 from Fekel & Balachandran (1993). A 100 K change in T_{eff} yields an ≈0.15 dex uncertainty, while a 2% change in the continuum level yields 0.10 dex.

The NLTE synthesis was also carried out with SME using MARCS model atmospheres but with pre-computed departure coefficients. The fit resulted in A(Li)$_{NLTE}$ = 1.27, in good agreement with the recent result by Rebull et al. (2015). We plot the LTE and the NLTE fits together in Fig. 3. Both the LTE and the NLTE approach yields abundances lower than the anticipated

Table 3. Temporal distribution of the Doppler images

Observing run	Doppler image	Mid-HJD 2 450 000+	Mid-date yyyy-mm-dd	Number of spectra	Data coverage [days]	Data coverage in P_{rot}
1st	S11	4154.266	2007-02-22	24	26.914	0.951
2nd	S21	4353.335	2007-09-09	23	26.968	0.953
	S22	4380.154	2007-10-06	20	26.957	0.953
	S23	4413.098	2007-11-08	27	42.950	1.518
	S24	4470.907	2008-01-05	21	36.000	1.272
	S25	4505.701	2008-02-09	19	45.969	1.624
3rd	S31	4785.477	2008-11-14	22	26.951	0.952
	S32	4820.173	2008-12-19	17	30.844	1.090
4th	S41	5146.236	2009-11-10	19	38.924	1.375
5th	S51	5616.227	2011-02-23	12	37.919	1.340
6th	S61	7408.699	2016-01-21	25	26.025	0.920
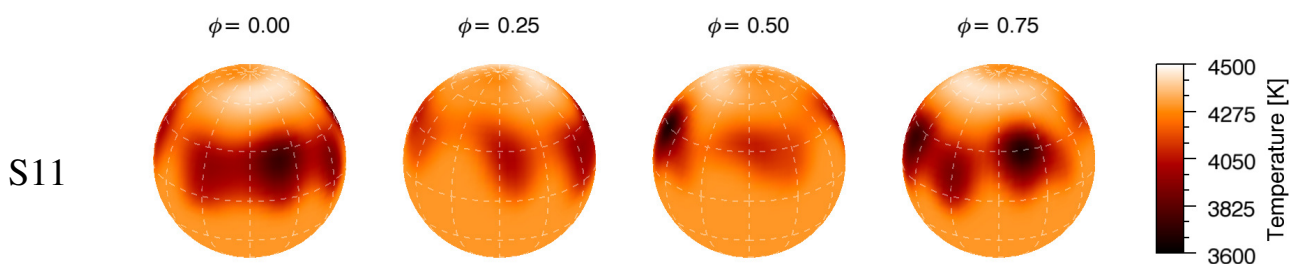
Fig. 4. Doppler image of V1192 Ori for the S11 data set. The corresponding mid-date is 2007-02-22. The spherical surface map is shown in four rotational phases (identified on top) along with the temperature scale.

limiting value of 1.5 for Li-rich giants. By applying the independent LTE-NLTE abundance correction of Klevas et al. (2016) to our LTE abundance yields $A(\mathrm{Li})_{\mathrm{NLTE}} = 1.46$, i.e. also below the nominal 1.5. Thus, we conclude that V1192 Ori is actually not a bona fide Li-rich giant but a Li-normal star with high surface amounts of Li.

6. Doppler images for 2007–2016

6.1. Configuring data subsets for Doppler imaging

Our spectroscopic data were taken during six observing runs between 2007 and 2016, each providing fairly good sampling for the relatively long rotational phase of 28.3 days. This data set allowed for altogether 11 Doppler reconstructions. Table 3 summarizes the temporal distribution of the Doppler reconstructions over the six runs (see also Table A.1 in the Appendix). The second and the third runs were long and continuous enough for obtaining Doppler images for several consecutive stellar rotations, suitable for studying surface differential rotation by tracking short-term spot displacements (see Sect. 7).

6.2. Image reconstruction code iMap

Our Doppler reconstruction code *iMap* performs multi-line inversion simultaneously for a large number of photospheric line profiles (Carroll et al. 2012). For the inversion we selected 40 suitable absorption lines from the 5000–6750 Å wavelength range by their line depth, blends, continuum level, and their temperature sensitivity (Künstler et al. 2015). Each contributing line

is modelled individually and locally and then disk-integrated; finally, all disk-integrated line profiles are averaged to form the mean line profile, which can be compared with each observed mean profile for each observed phase (for more details see Sect. 3 in Carroll et al. 2012).

The *iMap* code calculates the line profiles by solving the radiative transfer through an artificial neural network (Carroll et al. 2008). Atomic parameters are taken from the VALD database (Kupka et al. 1999). Model atmospheres are taken from Castelli & Kurucz (2004) and are interpolated for each desired temperature, gravity, and metallicity. Owing to the high workload for computation and modelling, we used LTE radiative transfer instead of spherical model atmospheres. Nevertheless, limitations from neglecting spherical model atmospheres and continuum scattering are compensated by using dense phase coverages (cf. Table 3) and also by using our multi-line approach. For the surface reconstruction *iMap* uses an iterative regularization based on a Landweber algorithm (Carroll et al. 2012), and therefore no additional constraints are imposed in the image domain. For the inversions we used the same stopping criteria as given by Carroll et al. (2012). According to our tests (see Appendix A in the aforementioned reference) the iterative regularization (i.e. step size control & stopping rule) is proved to be enough to converge always to the same image solution. The surface element resolution is set to $5° \times 5°$.

6.3. Doppler image reconstructions

Doppler reconstructions for V1192 Ori reveal a general characteristic; there are cool spots of different sizes and temperature
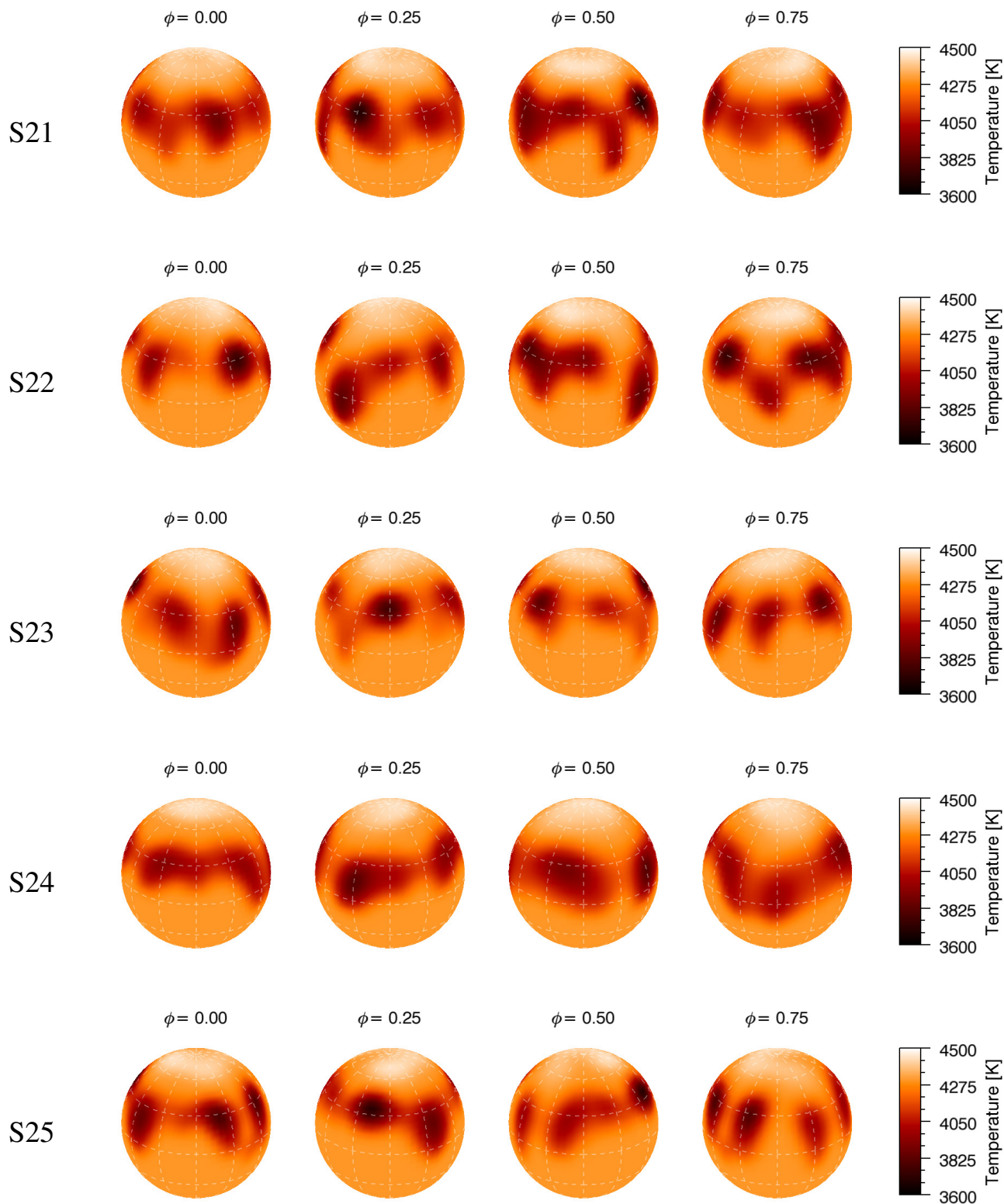
Fig. 5. Doppler images of V1192 Ori for the five data sets S21, S22, S23, S24, and S25. The corresponding mid-dates are 2007-09-09, 2007-10-06, 2007-11-08, 2008-01-05, and 2008-02-09 , respectively. Otherwise as in Fig. 4.

contrasts all around the equatorial regions within a belt extending not higher than ≈50° and a warm azimuthal belt at higher latitudes or partly covering the pole. The individual cool spots change in size considerably from one map to the next. The temperature of the coolest spots is ≈700 K below the effective temperature of the unspotted photosphere. On the other hand, no cool spots at all appear on or near the visible pole during the time of observations, but the high latitude or even polar patches of ≈150 K warmer regions are seen repeatedly. The overall surface structure with cool spots at lower latitudes and warmer but
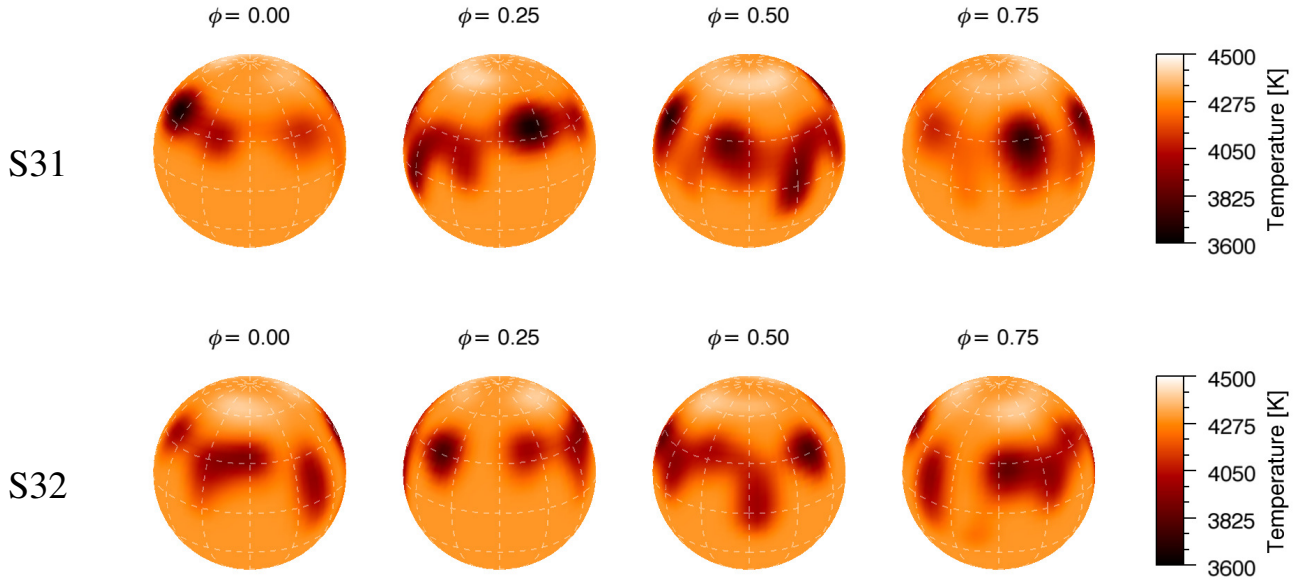
Fig. 6. Doppler images of V1192 Ori for the two data sets S31 and S32. The corresponding mid-dates are 2008-11-14 and 2008-12-19, respectively. Otherwise as in Fig. 4.
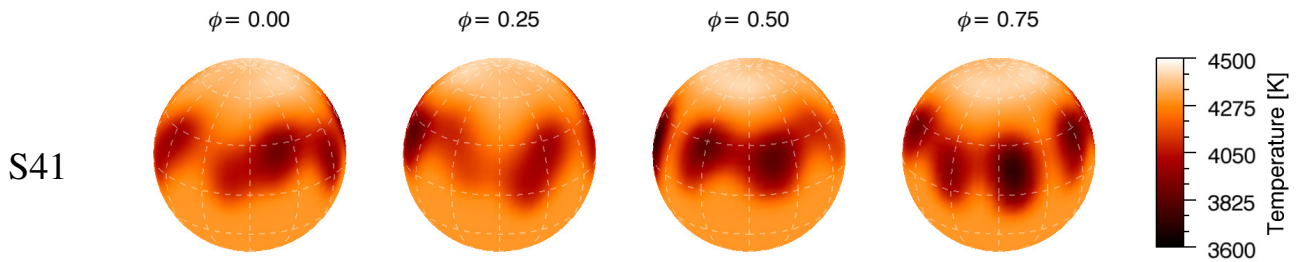

Fig. 7. Doppler image of V1192 Ori for the S41 data set. The corresponding mid-date is 2009-11-10. Otherwise as in Fig. 4.
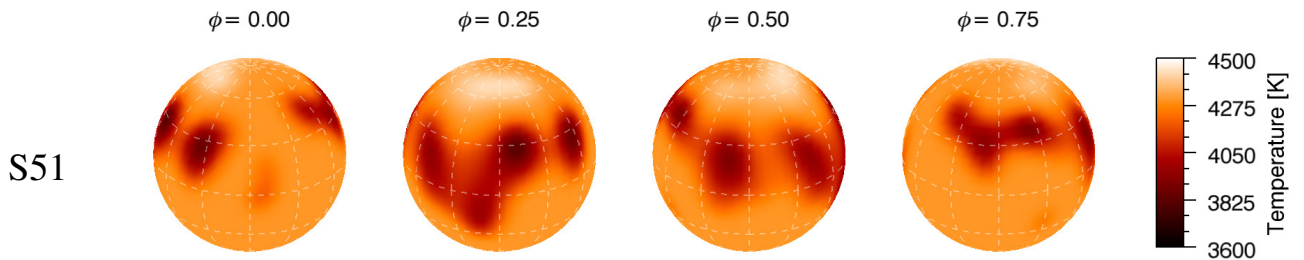

Fig. 8. Doppler image of V1192 Ori for the S51 data set. The corresponding mid-date is 2011-02-23. Otherwise as in Fig. 4.

weakly contrasted features at higher latitudes bears resemblance with the first Doppler images from late 1996 in Paper I, even though those maps revealed lower temperature contrasts. We evaluated the mean error for our temperature maps with a Monte Carlo analysis as described in Carroll et al. (2012) and found a maximum error of 110 K.

First run. The very first season in early 2007 is covered by a single data set that allowed only one surface reconstruction, shown in Fig. 4. It reveals a chain of relatively large, partly adjoined spots all around the star. The individual spots have different contrasts but are always cooler than the effective temper-

ature by ≈200–600 K. The azimuthal-shaped warm feature extends half around the pole to a longitude that coincides with the most prominent cool spot at lower latitudes, implying that there may be a connection or that the warm feature may only be an artifact or at least raises doubts about its reality.

Second run. The second season from late 2007 to early 2008 is our best-sampled season and provides five maps with a sampling of one map per stellar rotation. Again, as in early 2007, significant changes of the spot arrangement are seen from one map to the next. This is demonstrated in the time series of maps in Fig. 5. Nevertheless, the corresponding dominant spots can eas-
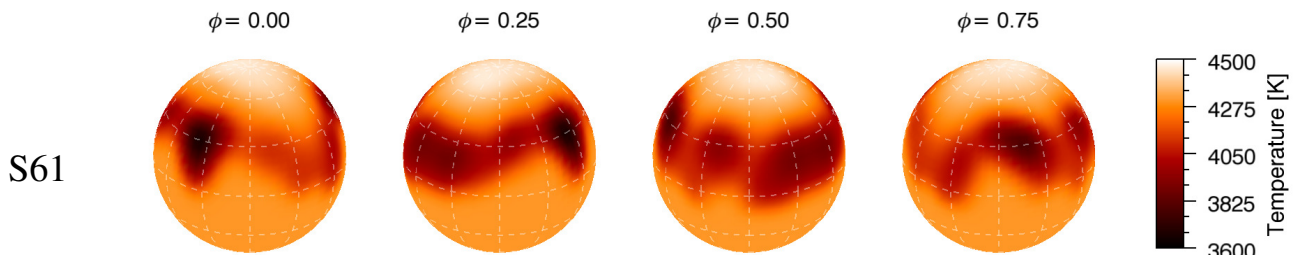
$\phi = 0.00$ $\phi = 0.25$ $\phi = 0.50$ $\phi = 0.75$

S61

Fig. 9. Doppler image of V1192 Ori for the S61 data set. The corresponding mid-date is 2016-01-21. Otherwise as in Fig. 4.

ily be tracked on the consecutive maps and, besides some degree of sporadic displacements, the longitudinal tracks already indicate significant differential surface rotation (cf. Sect. 7). This is particularly intriguing because the range of latitudes with spots as surface tracers is comparably narrow. There are also several other noteworthy morphological details, for example a persistent longitudinal gap between spots at around phase 0.4, or the one latitudinally displaced spot at "southern" latitude. At this point we point out that the Doppler-imaging technique would likely fail to resolve two close-together symmetric latitudinal belts of individual spots, for example as seen on our Sun. Simulations suggested that it likely reconstructs only a single belt placed at the sub-observers latitude (e.g. Rice & Strassmeier 2000).

Third run. For the third season in late 2008 (Fig. 6), we have another two consecutive maps. These maps again reveal spot rearrangements from one rotation to the next, which are partly morphological in nature and partly longitudinal migrations owing to differential surface rotation. The morphological changes were so rapid that there is almost no resemblance between the two maps; this is particularly the case, for example at phase 0.25 in Fig. 6, even though they are from two consecutive rotations. Such rapid variations are also seen on the Sun for particularly active spot groups, while solar plages may not even live as long as one solar rotation. Because the rotation periods of V1192 Ori and the Sun are not so different, 28.3 d versus 25 d, we may expect that some of the features we are mapping had evolved during the time of observation. If so, only a time average spot would be reconstructed.

Fourth, fifth, and sixth runs. Finally, for the rest of the data, namely from late 2009 (Fig. 7), early 2011 (Fig. 8), and early 2016 (Fig. 9) only one Doppler image per season was possible. Yet, each one shows basically the same morphology, i.e. cool spots at low to mid-latitudes distributed quasi-evenly along all rotational phases and weakly contrasted warm features at very high latitudes, but no cool spot at the pole itself.

7. Surface differential rotation from time-series Doppler images

The time-series Doppler images in the second and third observing season allowed us to study the surface differential rotation by means of a cross-correlation analysis of the consecutive maps. Our cross-correlation technique `ACCORD` (Kővári et al. 2015, and references therein) combines the available information from spot displacements in order to reconstruct the signature of the differential rotation. In the second season from late 2007 to early 2008, we have five consecutive Doppler images (dubbed S21, S22, S23, S24, and S25), while in late 2008, we have two (S31 and S32). Therefore, we are able to create altogether five image
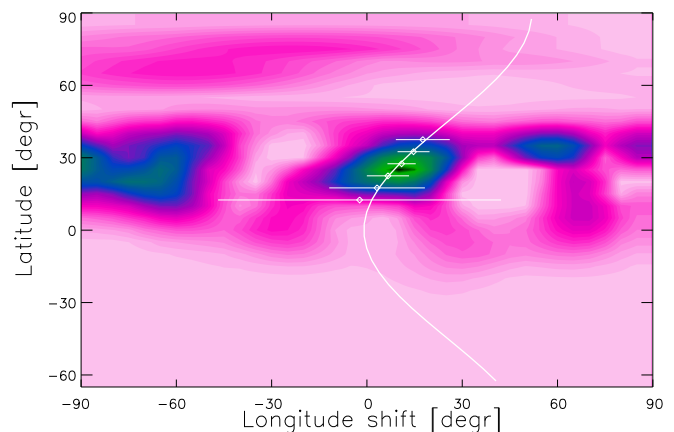
Fig. 10. Average cross-correlation map showing the evidence for surface differential rotation. Darker regions represent better correlation. The average longitudinal cross-correlation functions in 5° bins are fitted by Gaussian curves. Gaussian peaks are indicated by dots and the corresponding Gaussian widths by horizontal lines. The continuous line is the best fit, suggesting antisolar differential rotation with $P_{eq} = 28.35$ d equatorial period and $\alpha = -0.11$ surface shear.

pairs (S21-S22, S22-S23, S23-S24, S24-S25, and S31-S32) to be cross-correlated. These correlation maps are combined and the average correlation pattern is fitted with a quadratic rotation law. The result is shown in Fig. 10 and indicates antisolar differential rotation, i.e. on V1192 Ori the rotation rate increases from the equator towards the pole. Its rotation law is expressed in the form $\Omega(\beta) = \Omega_{eq}(1 - \alpha \sin^2 \beta)$, where $\Omega(\beta)$ is the angular velocity at β latitude, Ω_{eq} is the angular velocity at the equator, while α is the dimensionless surface shear coefficient obtained from $(\Omega_{eq} - \Omega_{pole})/\Omega_{eq}$, i.e. the angular velocity difference between the equator and the pole divided by the equatorial velocity. The best fit yields $\Omega_{eq} = 12.695 \pm 0.034°$/d and $\alpha = -0.11 \pm 0.02$. This can be converted to a lap time of ≈ 260 days, that is the time the polar regions need to lap the equator by one full rotation.

8. Summary and discussions

An extended Doppler imaging study with STELLA during the years 2007 to 2016 yielded 11 new surface image reconstructions, typically one image per stellar rotation. The 11 new Doppler images closely resemble the first Doppler image of V1192 Ori in Paper I from 1996-97 taken with a different telescope-spectrograph combination and with a different inversion code. Its surface spot distribution is well characterized in the sense that cool spots of different sizes and temperatures are

Table 4. Surface shear parameters obtained by cross-correlation of subsequent Doppler images

Star	Type	$P_{\rm rot}$ [d]	α surface shear	Reference
AB Dor	K0V, single	0.51	+0.005±0.001	Donati & Collier Cameron (1997)
LQ Hya	K2V, single	1.60	+0.006±0.001	Kővári et al. (2004)
EI Eri	G5IV, binary	1.94	+0.036±0.010	Kővári et al. (2009)
UZ Lib	K0III, binary	4.76	−0.027±0.009	Vida et al. (2007)
HU Vir	K0IV, binary	10.39	−0.029±0.005	Harutyunyan et al. (2016)
IL Hya	K0IV, binary	12.91	+0.05±0.01	Kővári et al. (2014)
DP CVn	K1III, single	14.01	−0.035±0.016	Kővári et al. (2013)
ζ And	K1III, binary	17.76	+0.055±0.002	Kővári et al. (2012)
DI Psc	K1III, single	18.02	−0.083±0.021	Kriskovics et al. (2014)
σ Gem	K1III, binary	19.60	−0.04±0.01	Kővári et al. (2015)
V2075 Cyg	K1III, binary	22.62	+0.015±0.003	Özdarcan et al. (2016)
KU Peg	K2III, single	23.90	+0.040±0.006	Kővári et al. (2016)
V1192 Ori	K2.5III, single	28.30	−0.11±0.02	this paper

always found within a relatively confined latitudinal belt extending up to ≈50° and centred at the sub-observers latitude. No cool spots appear on or near the visible polar region. On the other hand, the individual spots change dynamically, not only from one observing season to the next but from one rotation to the next and possibly even within a single stellar rotation. A warm feature appears consistently at high latitudes as a (partial) azimuthal ring around the pole but we are not certain of its reality. Even though there are now maps spanning 20 years, one cannot identify a clear cyclic behaviour or trend. Long-term variability is certainly present in the photometric light curve on a timescale of 5–10 years (Fig. 1). However, the 10-yr gap in the photometric data from March 1997 to March 2007 prevents us from suggesting any cycle length. We nevertheless refine the rotation period of V1192 Ori from these data to 28.30 days and derive a more reliable set of fundamental stellar parameters by comparing to updated evolutionary tracks. Accordingly, the spectral type of V1192 Ori is found to be K2.5III, i.e. 0.5 subclasses cooler than claimed earlier.

For the time-series Doppler images from the years 2007–2008, we applied our robust cross-correlation technique and found strong antisolar differential rotation with an $\alpha = -0.11$ surface shear coefficient. This result is in very good agreement with the earlier result of −0.12 from the independent data in Paper I. This is the case even though the α value in Paper I was derived only from a single cross-correlation of two consecutive Doppler maps, and therefore was significantly less robust and had larger error bars. With the present result, we are now confident that V1192 Ori indeed shows strong antisolar differential rotation. Together with DI Psc (Kriskovics et al. 2014) this is the strongest antisolar shear coefficient measured to date. Such strong shear supports the relation of $|\alpha| \propto P_{\rm rot}$, i.e. the lower the rotation the stronger the shear (Kővári & Oláh 2014). Also, a Rossby number of 0.22 derived for V1192 Ori (Aurière et al. 2015) indicates that an $\alpha\Omega$-type dynamo is operating underneath, i.e. differential rotation is expected to play an important role. Table 4 compares V1192 Ori to other measurements of differential surface rotation. The list is not complete and, for the sake of homogeneity, only results from Doppler-imaging studies applying the cross-correlation technique are listed.

The unusually fast rotation of a single, evolved star such as V1192 Ori can be explained in various ways, including angular momentum transport from the deep interior (Simon & Drake 1989). The mass of 1.85 $M_{\odot}$ found for V1192 Ori implies a precursor A5 spectral type on the main sequence (Ribas et al. 1997)

or even earlier in the case of a significant mass loss. Such a star does not have a deep outer convective zone to maintain a powerful magnetic dynamo that would result in effective magnetic braking on the main sequence (cf. Privitera et al. 2016a). Eventually this means more angular momentum conservation for the post-main sequence evolution, supporting the scenario of mixing up angular momentum. The position in the H-R diagram past the RGB luminosity bump (see Fig.2) indicates that V1192 Ori has completed Li production at the red-giant bump. According to Charbonnel & Balachandran (2000) the Li production is followed by an extra mixing phase, interconnecting the CN-burning zone with the convective envelope. Although the Li enrichment is relatively short lived, the extra mixing might explain the surface Li enrichment together with the peculiar rotation pattern. This is because freshly synthesized Li comes up to the surface along with high angular momentum material, which can eventually be conveyed towards the poles, resulting in the observed antisolar surface differential rotation (cf. Kitchatinov & Rüdiger 2004).

This scenario is also compatible with the Cameron-Fowler mechanism (Cameron & Fowler 1971) of Li production together with the so-called cool-bottom processes (Sackmann & Boothroyd 1999), which are thought to be responsible for bringing down material from the convective zone and exposing that material to higher temperatures in which partial nuclear fusion (H burning) occurs. Then, the Li-rich material is transported back to the convective zone by some circulation or diffusion, wherefrom convective mixing spreads it out towards the surface (see also Busso et al. 2007, and their references). The competing scenario of planet engulfment (cf. Mott et al. 2017, their Sect. 6 and the references therein) explains the existence of the ^{6}Li isotope in stellar atmospheres and may explain the rapid rotation as well, however, it would not easily account for antisolar differential rotation.

References

Allende Prieto, C. 2004, Astronomische Nachrichten, 325, 604
Aurière, M., Konstantinova-Antova, R., Charbonnel, C., et al. 2015, A&A, 574, A90
Aurnou, J., Heimpel, M., & Wicht, J. 2007, Icarus, 190, 110
Bidelman, W. P. & MacConnell, D. J. 1973, AJ, 78, 687
Bressan, A., Marigo, P., Girardi, L., Nanni, A., & Rubele, S. 2013, in European Physical Journal Web of Conferences, Vol. 43, European Physical Journal Web of Conferences, 03001
Bressan, A., Marigo, P., Girardi, L., et al. 2012, MNRAS, 427, 127
Busso, M., Wasserburg, G. J., Nollett, K. M., & Calandra, A. 2007, ApJ, 671, 802
Cameron, A. G. W. & Fowler, W. A. 1971, ApJ, 164, 111
Carroll, T. A., Kopf, M., & Strassmeier, K. G. 2008, A&A, 488, 781
Carroll, T. A., Strassmeier, K. G., Rice, J. B., & Künstler, A. 2012, A&A, 548, A95
Castelli, F. & Kurucz, R. L. 2004, ArXiv Astrophysics e-prints
Castilho, B. V., Gregorio-Hetem, J., Spite, F., Barbuy, B., & Spite, M. 2000, A&A, 364, 674
Charbonnel, C. & Balachandran, S. C. 2000, A&A, 359, 563
Charbonnel, C. & Lagarde, N. 2010, A&A, 522, A10
Csubry, Z. & Kolláth, Z. 2004, in ESA Special Publication, Vol. 559, SOHO 14 Helio- and Asteroseismology: Towards a Golden Future, ed. D. Danesy, 396
Cutri, R. M., Skrutskie, M. F., van Dyk, S., et al. 2003, VizieR Online Data Catalog, 2246
de La Reza, R., Drake, N. A., & da Silva, L. 1996, ApJ, 456, L115
de la Reza, R., Drake, N. A., da Silva, L., Torres, C. A. O., & Martin, E. L. 1997, ApJ, 482, L77
Donati, J.-F. & Collier Cameron, A. 1997, MNRAS, 291, 1
Dyck, H. M., Benson, J. A., van Belle, G. T., & Ridgway, S. T. 1996, AJ, 111, 1705
Fekel, F. C. 1988, in ESA Special Publication, Vol. 281, ESA Special Publication
Fekel, F. C. 1997, PASP, 109, 514
Fekel, F. C. & Balachandran, S. 1993, ApJ, 403, 708
Fekel, F. C., Moffett, T. J., & Henry, G. W. 1986, ApJS, 60, 551
Flower, P. J. 1996, ApJ, 469, 355
Gaia Collaboration, Brown, A. G. A., Vallenari, A., et al. 2016a, A&A, 595, A2
Gaia Collaboration, Prusti, T., de Bruijne, J. H. J., et al. 2016b, A&A, 595, A1
Gastine, T., Yadav, R. K., Morin, J., Reiners, A., & Wicht, J. 2014, MNRAS, 438, L76
Gezari, D. Y., Pitts, P. S., & Schmitz, M. 1999, VizieR Online Data Catalog, 2225
Gioia, I. M., Maccacaro, T., Schild, R. E., et al. 1990, ApJS, 72, 567
Granzer, T., Reegen, P., & Strassmeier, K. G. 2001, Astronomische Nachrichten, 322, 325
Gustafsson, B., Edvardsson, B., Eriksson, K., et al. 2008, A&A, 486, 951
Harutyunyan, G., Strassmeier, K. G., Künstler, A., Carroll, T. A., & Weber, M. 2016, A&A, 592, A117
Jofré, P., Heiter, U., Soubiran, C., et al. 2014, A&A, 564, A133
Jovanovic, M., Weber, M., & Allende Prieto, C. 2013, Publications de l'Observatoire Astronomique de Beograd, 92, 169
Käpylä, P. J., Käpylä, M. J., & Brandenburg, A. 2014, A&A, 570, A43
Kővári, Zs., Korhonen, H., Kriskovics, L., et al. 2012, A&A, 539, A50
Kővári, Zs., Korhonen, H., Strassmeier, K. G., et al. 2013, A&A, 551, A2
Kővári, Zs., Kriskovics, L., Künstler, A., et al. 2015, A&A, 573, A98
Kővári, Zs., Kriskovics, L., Oláh, K., et al. 2014, in IAU Symposium, Vol. 302, Magnetic Fields throughout Stellar Evolution, ed. P. Petit, M. Jardine, & H. C. Spruit, 379–380
Kővári, Zs., Künstler, A., Strassmeier, K. G., et al. 2016, A&A, 596, A53
Kővári, Zs. & Oláh, K. 2014, Space Sci. Rev., 186, 457
Kővári, Zs., Strassmeier, K. G., Granzer, T., et al. 2004, A&A, 417, 1047
Kővári, Zs., Washuettl, A., Foing, B. H., et al. 2009, in American Institute of Physics Conference Series, Vol. 1094, 15th Cambridge Workshop on Cool Stars, Stellar Systems, and the Sun, ed. E. Stempels, 676–679
Kirby, E. N., Guhathakurta, P., Zhang, A. J., et al. 2016, ApJ, 819, 135
Kitchatinov, L. L. & Rüdiger, G. 2004, Astronomische Nachrichten, 325, 496
Klevas, J., Kučinskas, A., Steffen, M., Caffau, E., & Ludwig, H.-G. 2016, A&A, 586, A156

Kriskovics, L., Kővári, Zs., Vida, K., Granzer, T., & Oláh, K. 2014, A&A, 571, A74
Künstler, A., Carroll, T. A., & Strassmeier, K. G. 2015, A&A, 578, A101
Kupka, F., Piskunov, N., Ryabchikova, T. A., Stempels, H. C., & Weiss, W. W. 1999, A&AS, 138, 119
Lindegren, L., Lammers, U., Bastian, U., et al. 2016, A&A, 595, A4
Mott, A., Steffen, M., Caffau, E., Spada, F., & Strassmeier, K. G. 2017, ArXiv e-prints
Oláh, K., Moór, A., Kővári, Z., et al. 2014, A&A, 572, A94
Özdarcan, O., Carroll, T. A., Künstler, A., et al. 2016, A&A, 593, A123
Piskunov, N. & Valenti, J. A. 2017, A&A, 597, A16
Privitera, G., Meynet, G., Eggenberger, P., et al. 2016a, A&A, 591, A45
Privitera, G., Meynet, G., Eggenberger, P., et al. 2016b, A&A, 593, A128
Rebull, L. M., Carlberg, J. K., Gibbs, J. C., et al. 2015, AJ, 150, 123
Reinhold, T. & Arlt, R. 2015, A&A, 576, A15
Ribas, I., Jordi, C., Torra, J., & Gimenez, A. 1997, A&A, 327, 207
Rice, J. B. & Strassmeier, K. G. 2000, A&AS, 147, 151
Sackmann, I.-J. & Boothroyd, A. I. 1992, ApJ, 392, L71
Sackmann, I.-J. & Boothroyd, A. I. 1999, ApJ, 510, 217
Schlegel, D. J., Finkbeiner, D. P., & Davis, M. 1998, ApJ, 500, 525
Simon, T. & Drake, S. A. 1989, ApJ, 346, 303
Slee, O. B., Nelson, G. J., Stewart, R. T., et al. 1987, MNRAS, 229, 659
Strassmeier, K. G., Bartus, J., Cutispoto, G., & Rodono, M. 1997a, A&AS, 125
Strassmeier, K. G., Boyd, L. J., Epand, D. H., & Granzer, T. 1997b, PASP, 109, 697
Strassmeier, K. G., Carroll, T. A., Weber, M., & Granzer, T. 2015, A&A, 574, A31
Strassmeier, K. G., Fekel, F. C., Bopp, B. W., Dempsey, R. C., & Henry, G. W. 1990, ApJS, 72, 191
Strassmeier, K. G., Granzer, T., Weber, M., et al. 2010, Advances in Astronomy, 2010, 19
Strassmeier, K. G., Kratzwald, L., & Weber, M. 2003, A&A, 408, 1103
Strassmeier, K. G., Serkowitsch, E., & Granzer, T. 1999, A&AS, 140, 29
van Belle, G. T., Lane, B. F., Thompson, R. R., et al. 1999, AJ, 117, 521
Vida, K., Kővári, Zs., Švanda, M., et al. 2007, Astronomische Nachrichten, 328, 1078
Voges, W., Aschenbach, B., Boller, T., et al. 1999, A&A, 349, 389
Vogt, S. S. & Hatzes, A. P. 1991, in Lecture Notes in Physics, Berlin Springer Verlag, Vol. 380, IAU Colloq. 130: The Sun and Cool Stars. Activity, Magnetism, Dynamos, ed. I. Tuominen, D. Moss, & G. Rüdiger, 297
Wasserburg, G. J., Boothroyd, A. I., & Sackmann, I.-J. 1995, ApJ, 447, L37
Weber, M., Granzer, T., & Strassmeier, K. G. 2012, in Society of Photo-Optical Instrumentation Engineers (SPIE) Conference Series, Vol. 8451, Society of Photo-Optical Instrumentation Engineers (SPIE) Conference Series, 0
Weber, M., Granzer, T., Strassmeier, K. G., & Woche, M. 2008, in Society of Photo-Optical Instrumentation Engineers (SPIE) Conference Series, Vol. 7019, Society of Photo-Optical Instrumentation Engineers (SPIE) Conference Series, 0
Weber, M. & Strassmeier, K. G. 2011, A&A, 531, A89
Worthey, G. & Lee, H.-c. 2011, ApJS, 193, 1

Appendix A: Observing log of the spectroscopic data and line profile fits for each individual surface reconstruction

Table A.1. Observing log of STELLA-SES spectra of V1192 Ori from 2007–2016 and grouping into subsets for Doppler reconstructions

HJD[a]	Phase[b]	Date	S/N	Subset	HJD[a]	Phase[b]	Date	S/N	Subset
4140.464	0.260	08.02.2007	253	S11	4382.641	0.818	09.10.2007	147	S22
4141.454	0.295	09.02.2007	296	S11	4383.644	0.853	10.10.2007	203	S22
4142.454	0.331	10.02.2007	274	S11	4384.638	0.888	11.10.2007	132	S22
4143.455	0.366	11.02.2007	298	S11	4387.646	0.995	14.10.2007	186	S22
4144.447	0.401	12.02.2007	185	S11	4388.658	0.030	15.10.2007	182	S22
4146.456	0.472	14.02.2007	309	S11	4389.635	0.065	16.10.2007	183	S22
4147.414	0.506	15.02.2007	264	S11	4390.614	0.099	17.10.2007	74	S22
4148.397	0.541	16.02.2007	267	S11	4392.647	0.171	19.10.2007	182	S22
4150.417	0.612	18.02.2007	283	S11	4393.646	0.207	20.10.2007	140	S22
4152.458	0.684	20.02.2007	279	S11	4395.630	0.277	22.10.2007	123	S23
4153.458	0.719	21.02.2007	278	S11	4396.614	0.311	23.10.2007	137	S23
4154.476	0.755	22.02.2007	252	S11	4398.579	0.381	25.10.2007	126	S23
4155.480	0.791	23.02.2007	275	S11	4399.574	0.416	26.10.2007	125	S23
4156.459	0.825	24.02.2007	186	S11	4400.698	0.456	27.10.2007	122	S23
4157.460	0.861	25.02.2007	158	S11	4402.601	0.523	29.10.2007	164	S23
4158.460	0.896	26.02.2007	253	S11	4403.584	0.558	30.10.2007	110	S23
4159.459	0.931	27.02.2007	240	S11	4404.677	0.596	31.10.2007	162	S23
4160.461	0.967	28.02.2007	237	S11	4405.591	0.629	01.11.2007	177	S23
4162.384	0.035	02.03.2007	323	S11	4406.607	0.665	02.11.2007	151	S23
4163.361	0.069	03.03.2007	262	S11	4412.639	0.878	08.11.2007	57	S23
4164.389	0.106	04.03.2007	304	S11	4412.711	0.880	08.11.2007	79	S23
4165.375	0.140	05.03.2007	263	S11	4413.659	0.914	09.11.2007	156	S23
4166.378	0.176	06.03.2007	294	S11	4414.550	0.945	10.11.2007	92	S23
4167.378	0.211	07.03.2007	303	S11	4414.704	0.951	10.11.2007	121	S23
4338.707	0.265	26.08.2007	144	S21	4416.545	0.016	12.11.2007	52	S23
4339.684	0.300	27.08.2007	136	S21	4416.622	0.018	12.11.2007	174	S23
4340.684	0.335	28.08.2007	101	S21	4417.562	0.052	13.11.2007	126	S23
4343.685	0.441	31.08.2007	145	S21	4417.687	0.056	13.11.2007	121	S23
4345.673	0.511	02.09.2007	131	S21	4418.583	0.088	14.11.2007	117	S23
4346.672	0.547	03.09.2007	137	S21	4419.578	0.123	15.11.2007	141	S23
4347.674	0.582	04.09.2007	122	S21	4420.574	0.158	16.11.2007	146	S23
4349.697	0.654	06.09.2007	151	S21	4421.578	0.194	17.11.2007	144	S23
4350.699	0.689	07.09.2007	151	S21	4422.683	0.233	18.11.2007	148	S23
4351.692	0.724	08.09.2007	141	S21	4423.575	0.264	19.11.2007	177	S23
4352.693	0.759	09.09.2007	162	S21	4437.679	0.763	03.12.2007	220	S23
4353.693	0.795	10.09.2007	129	S21	4438.580	0.794	04.12.2007	327	S23
4354.688	0.830	11.09.2007	145	S21	4450.470	0.214	15.12.2007	395	S24
4355.692	0.865	12.09.2007	155	S21	4459.403	0.530	24.12.2007	271	S24
4357.683	0.936	14.09.2007	156	S21	4460.401	0.565	25.12.2007	330	S24
4358.695	0.972	15.09.2007	107	S21	4461.402	0.601	26.12.2007	352	S24
4359.672	0.006	16.09.2007	153	S21	4462.394	0.636	27.12.2007	342	S24
4360.673	0.041	17.09.2007	137	S21	4463.399	0.671	28.12.2007	327	S24
4361.669	0.077	18.09.2007	133	S21	4464.408	0.707	29.12.2007	356	S24
4362.669	0.112	19.09.2007	153	S21	4465.388	0.742	30.12.2007	351	S24
4363.672	0.147	20.09.2007	144	S21	4466.386	0.777	31.12.2007	344	S24
4364.667	0.183	21.09.2007	131	S21	4467.406	0.813	01.01.2008	306	S24
4365.675	0.218	22.09.2007	122	S21	4468.379	0.847	02.01.2008	328	S24
4366.689	0.254	23.09.2007	137	S22	4469.589	0.890	04.01.2008	263	S24
4367.650	0.288	24.09.2007	55	S22	4471.443	0.956	05.01.2008	319	S24
4369.656	0.359	26.09.2007	108	S22	4475.452	0.097	09.01.2008	357	S24
4370.684	0.395	27.09.2007	149	S22	4479.446	0.238	13.01.2008	315	S24
4371.702	0.431	28.09.2007	166	S22	4481.448	0.309	15.01.2008	334	S24
4372.664	0.465	29.09.2007	164	S22	4482.456	0.345	16.01.2008	325	S24
4373.664	0.501	30.09.2007	139	S22	4483.452	0.380	17.01.2008	344	S24
4377.662	0.642	04.10.2007	138	S22	4484.418	0.414	18.01.2008	203	S24
4378.653	0.677	05.10.2007	126	S22	4485.438	0.450	19.01.2008	182	S24
4379.649	0.712	06.10.2007	158	S22	4486.470	0.487	20.01.2008	274	S24
4380.641	0.747	07.10.2007	161	S22	4488.410	0.555	22.01.2008	89	S25

[a] 2 450 000+
[b] Phases computed using Eq. 1.

Table A.1. continued.

| HJD[a]	Phase[b]	Date	S/N	Subset	HJD[a]	Phase[b]	Date	S/N	Subset
4488.481	0.558	22.01.2008	216	S25	5122.662	0.967	18.10.2009	299	S41
4490.497	0.629	24.01.2008	308	S25	5124.655	0.037	20.10.2009	149	S41
4491.452	0.663	25.01.2008	270	S25	5134.656	0.391	30.10.2009	292	S41
4492.389	0.696	26.01.2008	67	S25	5135.626	0.425	31.10.2009	336	S41
4494.422	0.768	28.01.2008	280	S25	5139.602	0.565	04.11.2009	318	S41
4495.407	0.802	29.01.2008	242	S25	5140.564	0.599	05.11.2009	126	S41
4496.454	0.839	30.01.2008	249	S25	5142.595	0.671	07.11.2009	270	S41
4499.444	0.945	02.02.2008	257	S25	5143.599	0.707	08.11.2009	250	S41
4501.456	0.016	04.02.2008	312	S25	5144.595	0.742	09.11.2009	273	S41
4502.457	0.052	05.02.2008	298	S25	5146.583	0.812	11.11.2009	323	S41
4508.460	0.264	11.02.2008	250	S25	5147.555	0.846	12.11.2009	146	S41
4512.461	0.405	15.02.2008	235	S25	5149.594	0.919	14.11.2009	225	S41
4514.462	0.476	17.02.2008	263	S25	5154.592	0.095	19.11.2009	251	S41
4515.461	0.511	18.02.2008	239	S25	5155.602	0.131	20.11.2009	279	S41
4516.461	0.546	19.02.2008	220	S25	5156.583	0.165	21.11.2009	159	S41
4532.378	0.109	06.03.2008	326	S25	5157.589	0.201	22.11.2009	268	S41
4533.379	0.144	07.03.2008	253	S25	5159.653	0.274	24.11.2009	315	S41
4534.379	0.179	08.03.2008	305	S25	5160.591	0.307	25.11.2009	307	S41
4774.642	0.669	04.11.2008	220	S31	5161.586	0.342	26.11.2009	256	S41
4775.595	0.703	05.11.2008	97	S31	5601.457	0.885	08.02.2011	72	S51
4775.639	0.705	05.11.2008	128	S31	5603.407	0.954	10.02.2011	96	S51
4775.726	0.708	05.11.2008	197	S31	5607.468	0.098	14.02.2011	107	S51
4776.644	0.740	06.11.2008	92	S31	5612.403	0.272	19.02.2011	114	S51
4776.733	0.743	06.11.2008	117	S31	5615.377	0.377	22.02.2011	115	S51
4777.595	0.774	07.11.2008	220	S31	5616.374	0.412	23.02.2011	113	S51
4778.595	0.809	08.11.2008	209	S31	5617.370	0.448	24.02.2011	139	S51
4779.590	0.844	09.11.2008	283	S31	5618.370	0.483	25.02.2011	110	S51
4780.586	0.879	10.11.2008	264	S31	5619.377	0.519	26.02.2011	91	S51
4781.670	0.918	11.11.2008	130	S31	5620.379	0.554	27.02.2011	59	S51
4783.586	0.985	13.11.2008	208	S31	5623.371	0.660	02.03.2011	122	S51
4784.581	0.021	14.11.2008	260	S31	5639.376	0.225	18.03.2011	94	S51
4785.581	0.056	15.11.2008	256	S31	7396.439	0.312	08.01.2016	182	S61
4789.583	0.197	19.11.2008	240	S31	7397.478	0.349	09.01.2016	387	S61
4793.594	0.339	23.11.2008	222	S31	7398.456	0.384	10.01.2016	364	S61
4794.588	0.374	24.11.2008	229	S31	7399.476	0.420	11.01.2016	359	S61
4795.584	0.409	25.11.2008	232	S31	7400.476	0.455	12.01.2016	372	S61
4798.671	0.518	28.11.2008	228	S31	7401.474	0.490	13.01.2016	196	S61
4799.533	0.549	28.11.2008	225	S31	7402.526	0.527	14.01.2016	324	S61
4800.593	0.586	30.11.2008	252	S31	7403.585	0.565	16.01.2016	200	S61
4801.593	0.622	01.12.2008	214	S31	7404.503	0.597	16.01.2016	350	S61
4805.597	0.763	05.12.2008	218	S32	7406.523	0.669	18.01.2016	365	S61
4808.589	0.869	08.12.2008	232	S32	7407.477	0.702	19.01.2016	406	S61
4809.663	0.907	09.12.2008	245	S32	7408.503	0.739	20.01.2016	395	S61
4810.591	0.940	10.12.2008	173	S32	7409.461	0.772	21.01.2016	361	S61
4811.596	0.975	11.12.2008	222	S32	7410.461	0.808	22.01.2016	326	S61
4812.595	0.010	12.12.2008	183	S32	7411.463	0.843	23.01.2016	370	S61
4814.603	0.081	14.12.2008	164	S32	7412.485	0.879	24.01.2016	377	S61
4817.606	0.187	17.12.2008	220	S32	7413.499	0.915	25.01.2016	364	S61
4818.494	0.219	17.12.2008	246	S32	7414.464	0.949	26.01.2016	405	S61
4819.470	0.253	18.12.2008	141	S32	7415.463	0.985	27.01.2016	390	S61
4822.479	0.360	21.12.2008	234	S32	7416.489	0.021	28.01.2016	187	S61
4827.430	0.535	26.12.2008	65	S32	7418.476	0.091	30.01.2016	361	S61
4828.460	0.571	27.12.2008	229	S32	7419.485	0.127	31.01.2016	242	S61
4829.451	0.606	28.12.2008	147	S32	7420.453	0.161	01.02.2016	69	S61
4834.442	0.782	02.01.2009	293	S32	7421.441	0.196	02.02.2016	195	S61
4835.440	0.818	03.01.2009	236	S32	7422.464	0.232	03.02.2016	277	S61
4836.441	0.853	04.01.2009	232	S32					

[a] 2 450 000+
[b] Phases computed using Eq. 1.
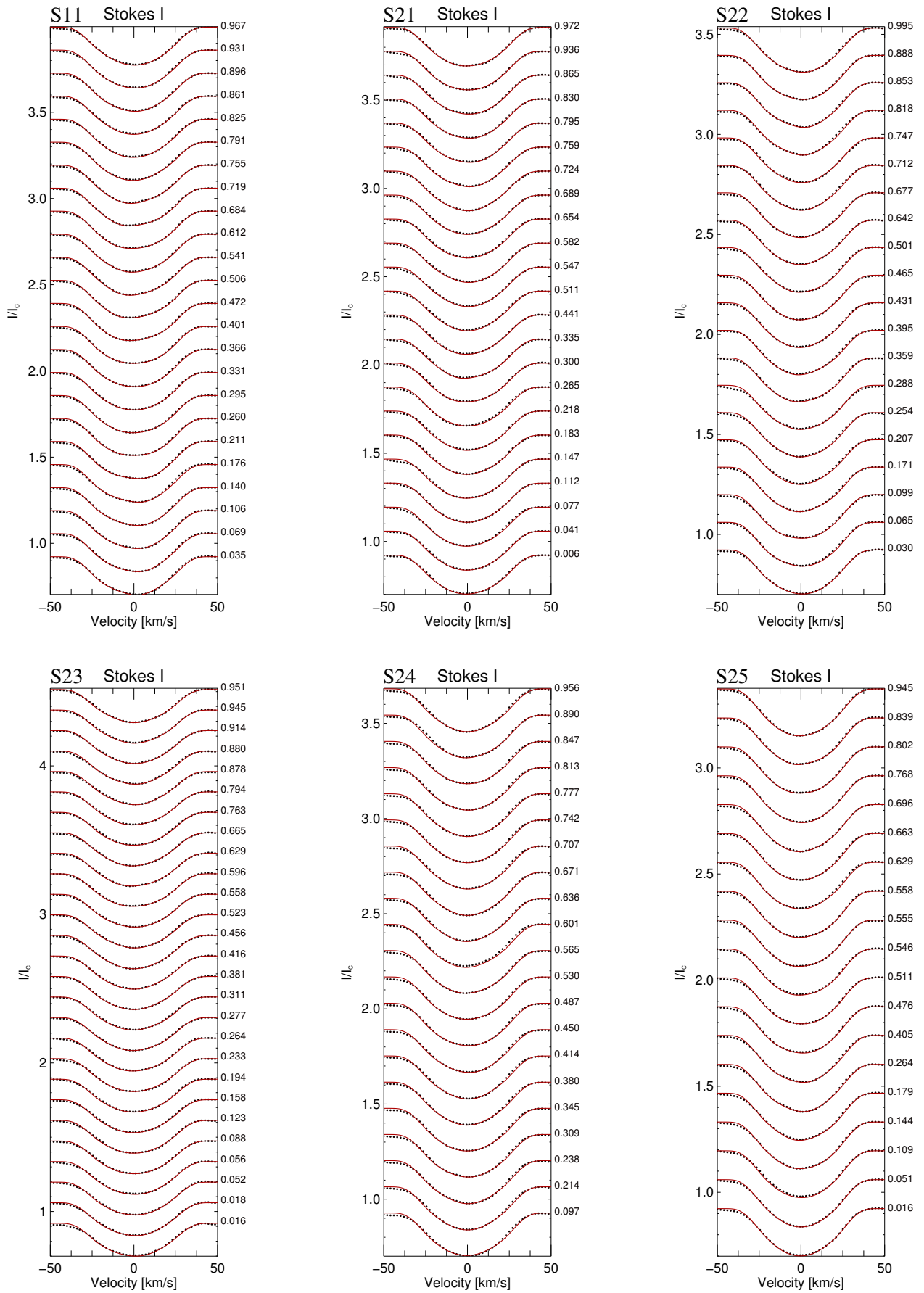
Fig. A.1. Line profile fits for the Doppler reconstructions shown in Figs. 4–5. The phases of the individual observations are listed on the right side of the panels.
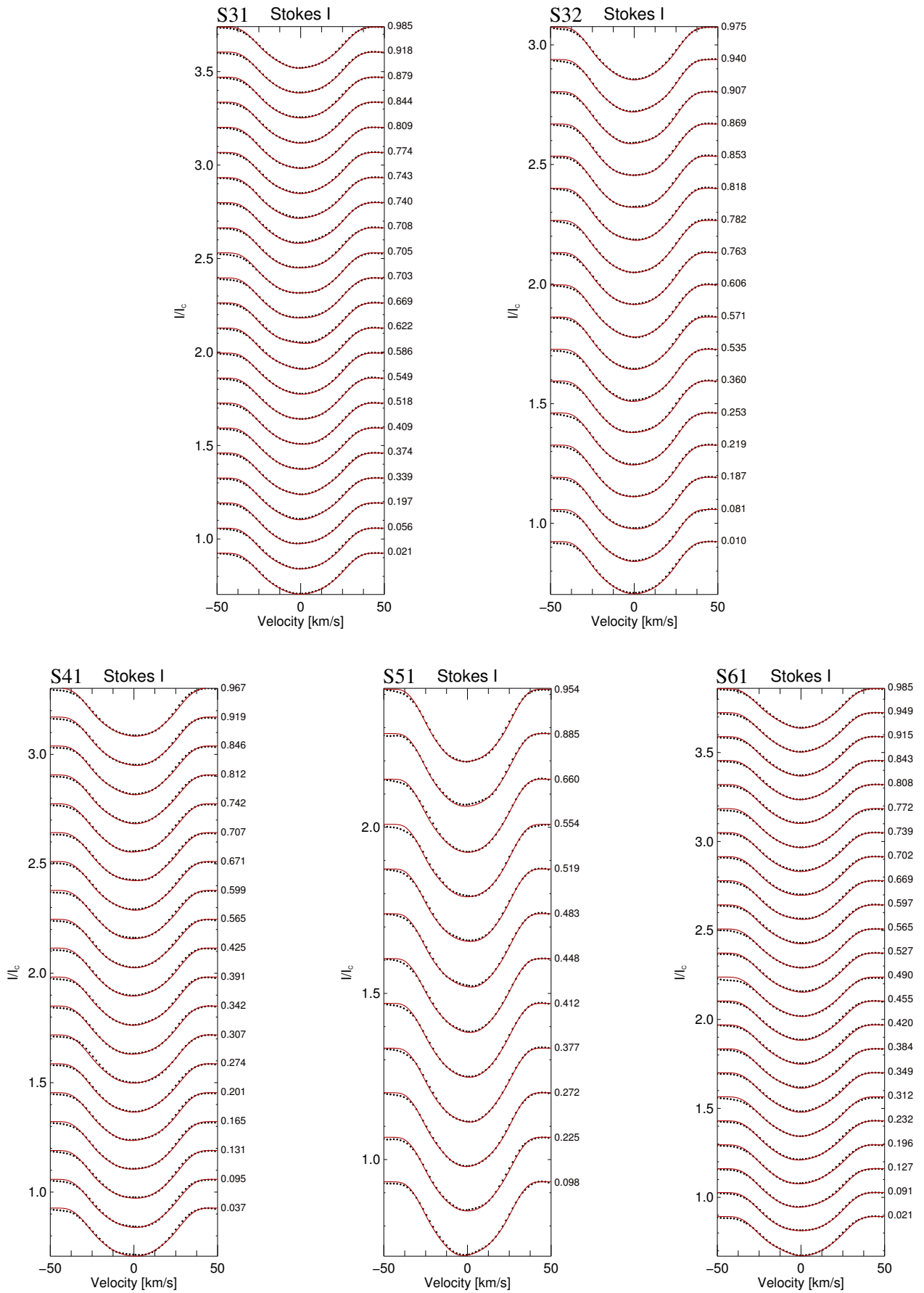
Fig. A.2. Line profile fits for the Doppler reconstructions shown in Figs. 6–9. The phases of the individual observations are listed on the right side of the panels.